JOURNAL OF AIRCRAFT
Vol. 38, No. 2, March–April 2001

Effect of Compressibility on Suppression of Dynamic Stall Using a Slotted Airfoil

L. W. Carr*
NASA Ames Research Center, Moffet Field, California 94035
M. S. Chandrasekhara†
Naval Postgraduate School, Monterey, California 93943
M. C. Wilder‡
Eloret, Sunnyvale, California
and
K. W. Noonan§
NASA Langley Research Center, Virginia 23681-0001

A multielement airfoil designed for helicopter application has been tested for compressible dynamic stall behavior and has been proven to be a robust dynamic stall-free concept. This slotted airfoil has operated into poststall areas without the dynamic stall vortex that is normally present whenever airfoils are tested beyond their static stall boundary. Point diffraction interferogram images of the dynamic flow over the airfoil are presented, showing details of the flow development during the oscillation cycle, and instantaneous pressure distributions on the airfoil and slat during dynamic airfoil motion are included.

Nomenclature

C_d	=	drag coefficient
C_l	=	airfoil lift coefficient
$C_{l_{\max}}$	=	maximum airfoil lift coefficient
C_M	=	pitching moment coefficient
C_p	=	pressure coefficient
$C_{p_{\min}}$	=	peak suction pressure coefficient
c	=	airfoil chord
f	=	frequency of oscillation, Hz
k	=	reduced frequency, $\pi f c/U_\infty$
M	=	freestream Mach number
Re	=	Reynolds number based on chord
U_∞	=	freestream velocity
x, y	=	chordwise and vertical distance
α	=	angle of attack
α_a	=	amplitude of oscillation
α_0	=	mean angle of attack
ω	=	circular frequency, rad/s

I. Introduction

DYNAMIC stall effects significantly limit the range of angles of attack that helicopter rotor blade airfoils are permitted to operate, thereby limiting the maneuver performance of modern-day helicopters. The airfoil sections used on modern-day helicopters are the result of decades of optimization and refinement, and the performance of these airfoils is dramatically better than the airfoils first used on helicopters. However, requirements for performance of future generations of military helicopters will exceed the capabilities of even these present-day single-element airfoils. Therefore, a major effort is underway focusing on the development of advanced airfoil concepts for helicopter rotor blade applications.

Over the years, many studies have been performed in an effort to better understand the physics and characteristics of dynamic stall (see Carr,[1] Carr and McCroskey,[2] and Carr and Chandrasekhara[3] for reviews). As more information about and greater understanding of the dynamic stall process has been developed, efforts have focused on ways to delay formation of the dynamic stall vortex to higher angles of attack, or even to eliminate it from the operating environment of the helicopter. One particularly robust technique was demonstrated by Carr and McAlister,[4] where an airfoil with a fixed slat optimized for steady high-lift conditions was tested for dynamic stall behavior. As shown in Ref. 4, the dynamic stall vortex formation was delayed to extremely high angle of attack for a VR-7 airfoil; at some conditions, no dynamic stall vortex was observed at any angle lower than 34 deg. As can be seen in Fig. 1, suppression of the dynamic stall vortex resulted in elimination of the pitching moment excursions that are the primary reason that dynamic stall conditions must be avoided.

The dynamic stall study of this slotted airfoil configuration demonstrated that there is indeed a way to suppress the dynamic stall vortex; however, this design was only optimized for dynamic stall at moderate Mach numbers ($M = 0.185$); it was not conceived as an optimum for all flight regimes of the rotor because of the higher drag. Therefore, a set of experiments was performed to establish the performance characteristics of slotted airfoils at transonic speed. In a test applying a slot to a state-of-the-art helicopter airfoil, Noonan et al.[5] tested two slot configurations on a RC(6)-608 airfoil at various steady transonic speeds and found that these airfoil configurations produced 29–61% higher lift than the basic airfoil at high speed, but suffered from higher drag at low angles of attack.

The slotted airfoil results were sufficiently promising to justify a test on a model rotor at high forward speed. In this test, rotor blades were constructed such that the outer section of the blade could be replaced by sections constructed in the slot configuration, as well as other high-lift designs.[6] The rotor with conventional airfoils was limited to a range of $C_T/\sigma \sim$ 0.07-0.1 (where C_T/σ is the rotor lift, which has been nondimensionalized in rotor terminology by the rotor swept area rather than airfoil chord). This produces an average lift coefficient of 0.42 at C_T/σ value of 0.07 and is generally sufficient to sustain a one-g level flight. This limitation was imposed by vibratory loads, which increased dramatically as higher lift was

Presented as Paper 98-0332 at the AIAA 36th Aerospace Sciences Meeting and Exhibit, Reno, NV, 12–15 January 1998; received 4 August 1999; revision received 28 November 2000; accepted for publication 29 November 2000.

*Emeritus Scientist, Aeroflightdynamics Directorate, U.S. Army Aviation and Missile Command. Senior Member AIAA.
†Research Professor and Associate Director, Navy–NASA Joint Institute of Aeronautics, Department of Aeronautics and Astronautics. Associate Fellow AIAA.
‡Senior Research Scientist, 625 Clyde Avenue. Member AIAA.
§Research Scientist, Aeroflightdynamics Directorate, U.S. Army Aviation and Missile Command.

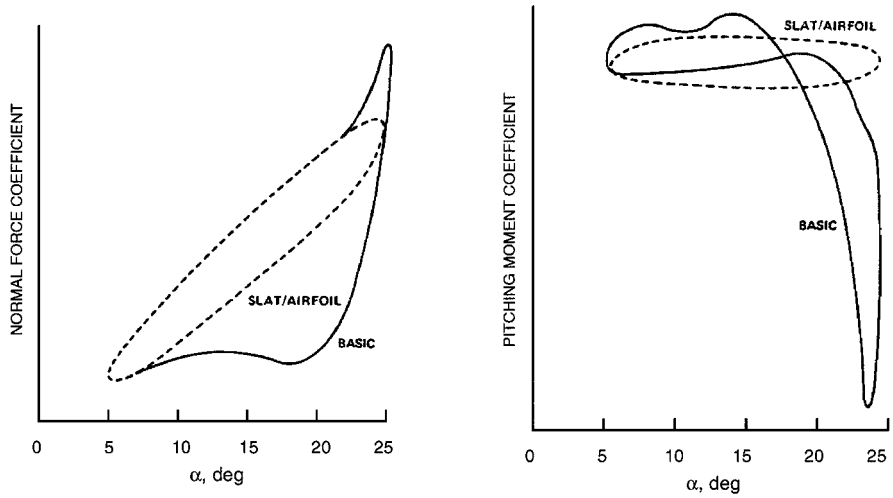

Fig. 1 Comparison of adjusted lift and pitching moment coefficients for basic VR-7 and slat/airfoil combination, $k = 0.05$, $\alpha = 15$ deg + 10 deg sin ωt, $Re = 2.5 \times 10^6$, and $M = 0.186$ (Ref. 4).

attempted. The rotor with the slotted airfoil could be operated at 20% greater lift values than the basic configuration, thus demonstrating that the slotted airfoil concept was indeed effective on the rotor. Generally model rotors could be operated at C_T/σ of 0.1–0.15.

Thus, it is clear that slotted airfoils do indeed affect the high-lift performance of helicopters. However, as also noted, slotted airfoils have higher drag at low angles of attack, especially on the advancing side where the Mach number is high. It is also not practical to use mechanical, electromechanical or other devices to overcome this limitation. Therefore, an optimization effort is needed to ensure good dynamic stall performance while maintaining good high-speed performance at the same time. If this is to be achieved, much more information is needed about the character of the dynamic stall delay achieved by the slotted airfoil across a range of Mach numbers. In an effort focused on this task, models of these airfoils were built for study in the Compressible Dynamic Stall Facility (CDSF) at the NASA Ames Research Center Fluid Mechanics Laboratory. Dynamic stall tests across a range of Mach numbers and reduced frequencies were pursued to assess quantitatively the dynamic stall behavior at the Mach numbers and Reynolds numbers experienced by the model rotor. The first findings of this study are presented in the present paper.

II. Description of the Facility and Experiment

A. Design of Models

Design efforts[7] have resulted in very efficient single-element airfoils tailored specifically for helicopter rotor blade applications. One of these airfoils, the RC(6)-08, an 8% thick airfoil section, has been studied extensively in steady flow across a wide range of Mach numbers in wind-tunnel tests.[5] These tests demonstrated significant improvements in $C_{l_{\max}}$ ($C_{l_{\max}} \geq 1.0$ at $M = 0.40$, $Re = 5.0 \times 10^6$) as well as good drag divergence Mach number behavior ($M_{dd} \geq 0.85$). Therefore, this airfoil was chosen as the reference airfoil for the study of slot design.

Two slot configurations were evaluated in steady flow.[5] Figure 2 shows $C_{l_{\max}}$ vs Mach number performance for these configurations. The slotted airfoils were identified by the baseline airfoil plus configuration numbers. In this connotation, RC(6)-08/210 is explained as rotorcraft (RC), airfoil series number (6), maximum thickness in percent of airfoil chord -08, and choice of pivot point for the slat first digit and negative of the slat rotation angle second and third digits/210 (see Ref. 5 for details).

In the present dynamic stall study, the basic RC(6)-08 and two slat configurations, RC(6)-08/106 and RC(6)-08/210, were tested; these profiles are shown in Fig. 3. Specially constructed models were built for dynamic stall testing: The single-element airfoil and a main airfoil with the two leading-edge configurations outlined earlier. These models were built to the standards set for dynamic stall tests in the CDSF; each model fits between the optical glass windows described next.

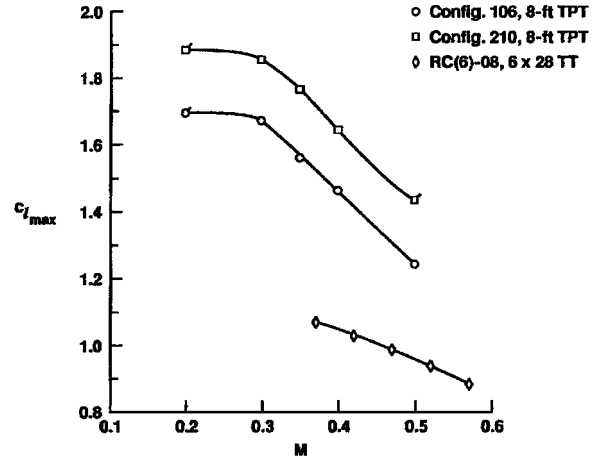

Fig. 2 Comparison of maximum lift coefficients for basic and two slotted airfoils as a function of Mach number.[5]

B. Design of Tunnel

The CDSF is an indraft wind tunnel[8] with a 10×14 in. test section and is equipped with a drive for producing a sinusoidal variation of the airfoil angle of attack. The flow in the tunnel is controlled by a choked, variable-area throat downstream of the test section, to produce a Mach number range of $0 < M < 0.5$. The flow is produced by a 6-MW, 240,000 cubic feet per minute, continuously running evacuation compressor. The airfoil mean angle of attack α_m can be set to $0 \leq \alpha_m \leq 15$ deg, the amplitude of oscillation α_a to $2 \leq \alpha_a \leq 10$ deg, and the oscillation frequency f to $0 \leq f \leq 100$ Hz. The uniqueness of the CDSF is that a 3-in. chord airfoil is supported between two 6-in. diam optical glass windows by small pins to permit direct optical access to the airfoil surface everywhere, for flow exploration using nonintrusive diagnostic techniques.

C. Description of Point Diffraction Interferometry Technique

The experimental data were obtained using the real-time technique of point diffraction interferometry (PDI). It provides detailed, instantaneous, quantitative, flowfield density information, from which both surface and global pressure distributions can be derived. The PDI optics are similar to those of a schlieren system, but as shown in Fig. 4, a laser light source (Quantronix continuous wave/pumped Nd-YAG laser) is used with a beam expander to fill

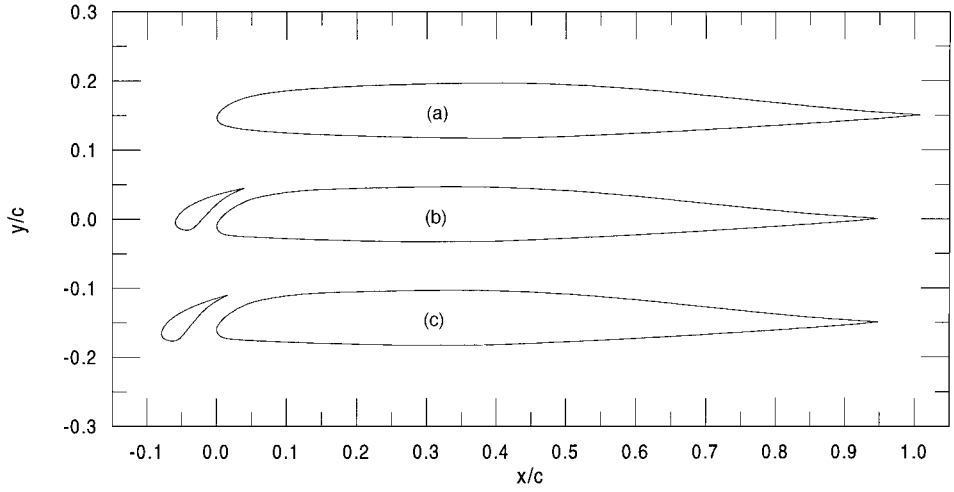

Fig. 3 Profile of models used in slotted airfoil experiments: a) basic RC(6)-08, b) RC(6)-08/106 with 6-deg slat, and c) RC(6)-08/210 with 10-deg slat.

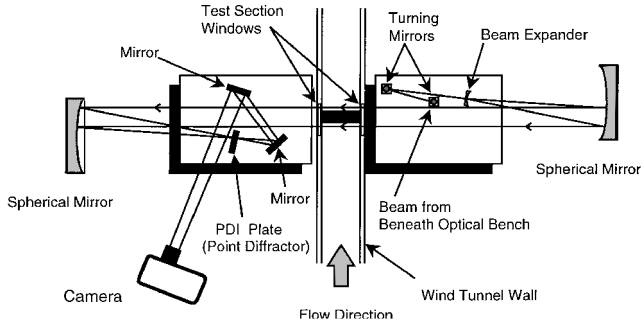

Fig. 4 Schematic of the PDI system.

the entire field (determined by the tunnel windows) of view in the standard Z-type configuration. The optics is aligned to minimize astigmatism. A photographically developed but not fixed, partially transmitting, holographic film plate replaces the knife edge. As in other interferometry techniques, the PDI technique requires a reference beam and a signal beam to interfere to form an image. However, unlike other techniques, the reference beam is derived from the signal beam using a single-pass approach through the optics (described subsequently). The reference beam is produced by diffracting light from a point source (pinhole) created on this holographic plate. The point source is formed, under no-flow conditions, by burning away the emulsion locally where the intense laser beam energy is focused from the second spherical mirror in Fig. 4. This in situ creation of the point diffracting spot makes the technique self-aligning. When the tunnel flow is on, light passing through the tunnel and phase shifted by the flow density changes (signal beam) focuses around the pinhole to an image size slightly larger than the spot. Thus, the light around the pinhole is transmitted through the plate remains as the signal beam, while that passing through the pinhole becomes the reference beam due to the spatial filtering characteristics of the pinhole. These two beams then interfere to produce fringes in real time. The contrast and sharpness of the fringes depends on the optical density of the holographic plate and differs with Mach number. Imaging optics is set up farther along the beam path to enable recording the flow interferograms on Polaroid film. In Ref. 9, the technique and its implementation in the CDSF is fully described. The technique has now evolved to an extent that several hundred interferograms can be recorded in a day's work.

D. Test Conditions and Data Acquisition

Dynamic stall on a rotor appears at conditions where the rotor blade locally exceeds the static stall angle. On most modern helicopters under heavy load or maneuver, the static stall angle is exceeded when the rotor blade is in the vicinity of 210–230 deg azimuth, with $M \cong 0.40$. Therefore, tests of the slotted configuration ranged over $0.2 \leq M \leq 0.45$ and reduced frequency $0 \leq k \leq 0.10$, for $\alpha = 10 \text{ deg} + 10 \text{ deg} \sin \omega t$. To reduce the experimental uncertainties to a minimum, two fields of view were captured whenever possible; full images were obtained in virtually all cases, with magnified leading-edge images obtained wherever needed.

Interferometric images were obtained at closely spaced angles of attack, chosen such that all characteristics of the flow development were captured on film. These images were then processed to quantitatively map the interference fringe intersections with the slat and the main airfoil surfaces, and pressure distributions were then deduced from this analysis.

E. Experimental Uncertainties

The following are the estimated uncertainties in the various quantities: Mach number: 0.005, angle of attack: 0.1 deg, reduced frequency: 0.5% at rates <30 rad/s and 1% at rates >30 rad/s, C_p at $M = 0.20$: 0.225, at $M = 0.30$: 0.075, and at $M = 0.45$: 0.0375. The uncertainty in C_p is estimated to be one fringe ($\Delta C_p \cong 0.1$ at $M = 0.30$) for the flow in general with about three fringes possibly undetectable for the peak suction pressure coefficient.

III. Results and Discussion

A. Discussion of Interferograms

Interferograms were obtained for a wide range of test conditions for the three airfoils tested in this study. These interferograms provide a quantitative visualization of the developing flow on and around the airfoils during oscillation at these compressible flow speeds. Because the fringes map lines of constant density and, therefore, pressure,[10] they offer some insight into the physics of this developing flow.

1. Dynamic Stall on the Basic RC(6)-08 Airfoil

For the range $0.2 < M < 0.4$, the dynamic stall process on the basic RC(6)-08 airfoil is similar to that observed on the NACA0012 airfoil that has been extensively tested in previous experiments in the compressible dynamic stall program, and the reader is referred to Ref. 3 to learn more about the physics of single-element airfoil dynamic stall. From the present study, the flow on the RC(6)-08 airfoil during oscillation at $k = 0.05$ and $M = 0.25$ is presented in Fig. 5a–5f. In Figs. 5–15, the right column shows leading-edge flow details either as captured or as an enlarged view of the image on the left. The flow is fully attached at $\alpha = 13.5$ deg, the last angle before onset of dynamic stall, as can be seen clearly from the interferogram presented in Figs. 5a and 5b. Here the rapid acceleration of the flow around the leading edge is evident by the high number of fringes

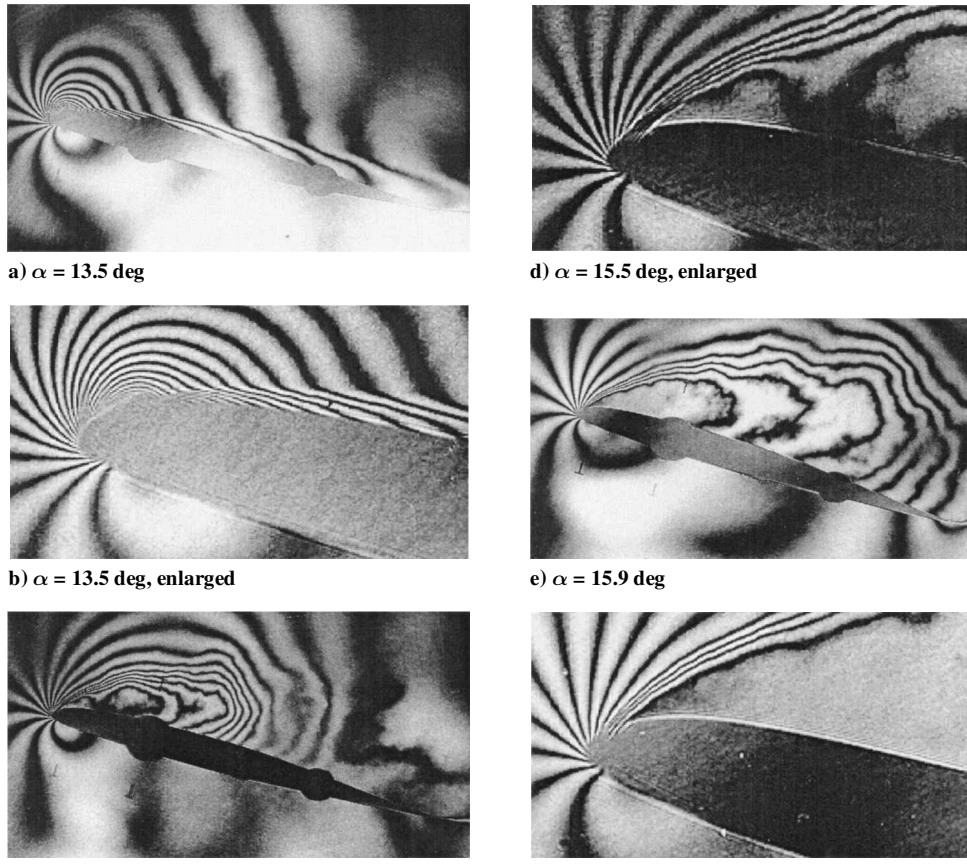

a) α = 13.5 deg

d) α = 15.5 deg, enlarged

b) α = 13.5 deg, enlarged

e) α = 15.9 deg

c) α = 15.5 deg

f) α = 15.9 deg, enlarged

Fig. 5 Interferograms showing instantaneous flow conditions during pitch oscillation of the basic RC(6)-08 airfoil at k = 0.05 and M = 0.25.

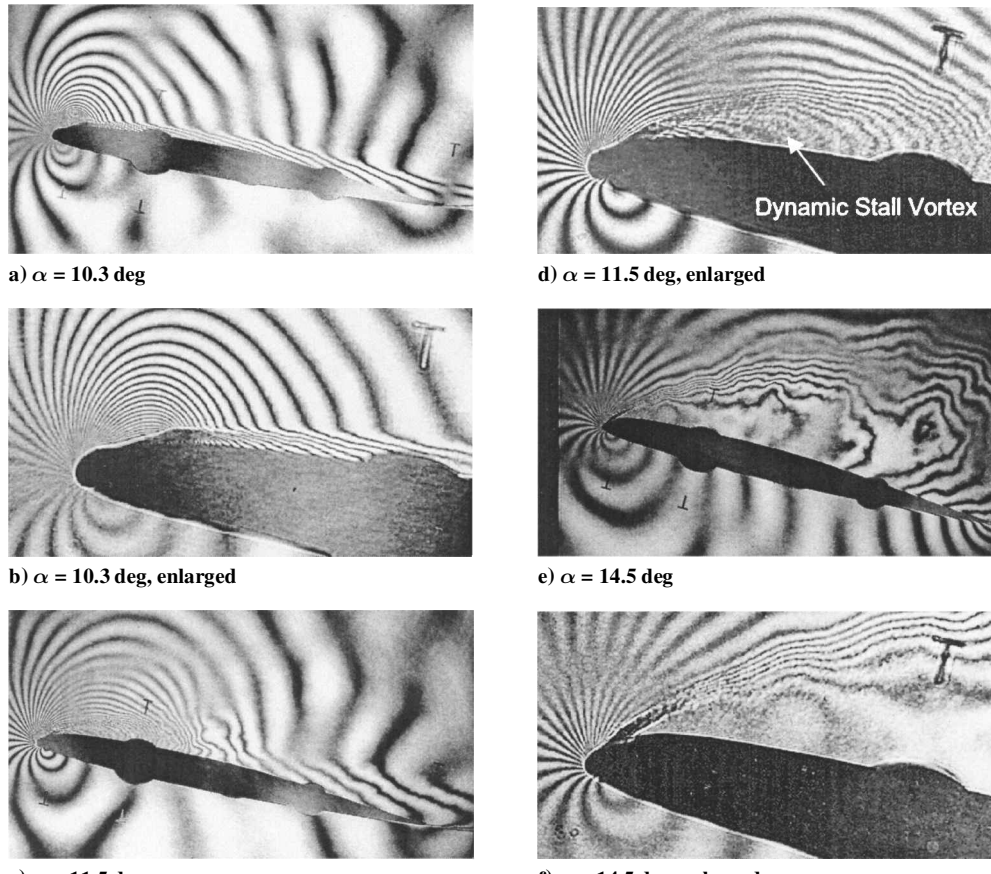

a) α = 10.3 deg

d) α = 11.5 deg, enlarged

b) α = 10.3 deg, enlarged

e) α = 14.5 deg

c) α = 11.5 deg

f) α = 14.5 deg, enlarged

Fig. 6 Interferograms showing instantaneous flow conditions during pitch oscillation of the basic RC(6)-08 airfoil at k = 0.05 and M = 0.40.

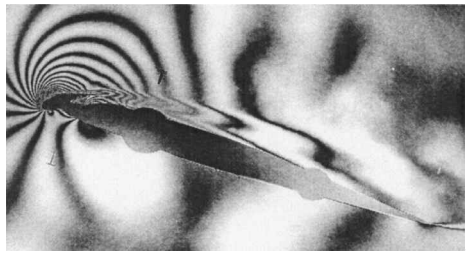

a) α = 18.5 deg

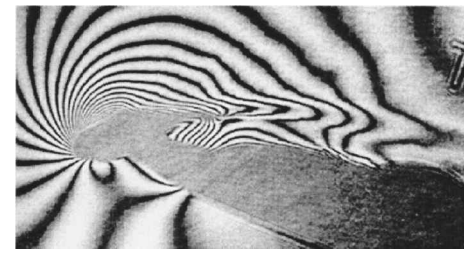

d) α = 20.0 deg, enlarged

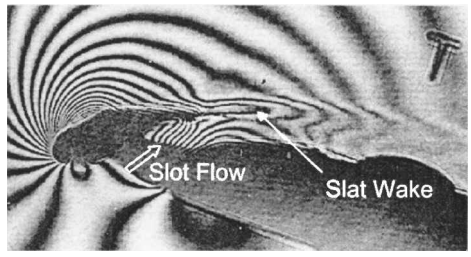

b) α = 18.5 deg, enlarged

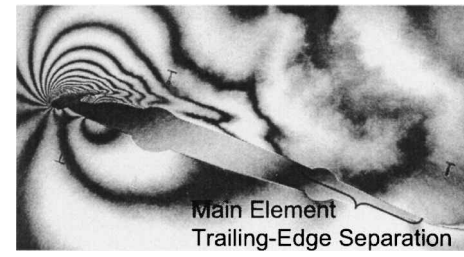

e) α = 18.5 deg on downstroke

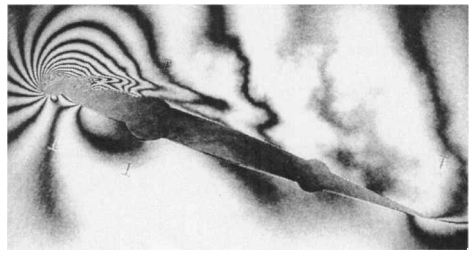

c) α = 20.0 deg

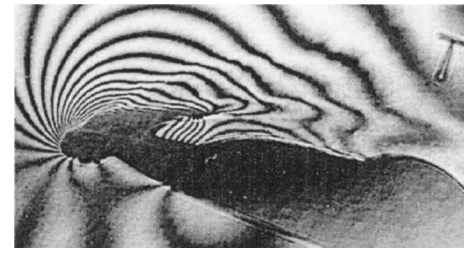

f) α = 18.5 deg on downstroke, enlarged

Fig. 7 Interferograms showing instantaneous flow conditions during pitch oscillation of the slotted airfoil configuration RC(6)-08/210 at k = 0.05 and M = 0.25.

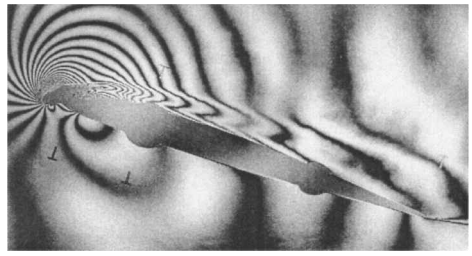

a) α = 18.0 deg

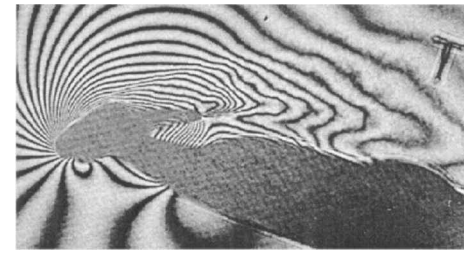

d) α = 19.0 deg, enlarged

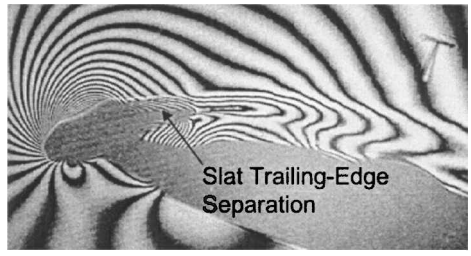

b) α = 18.0 deg, enlarged

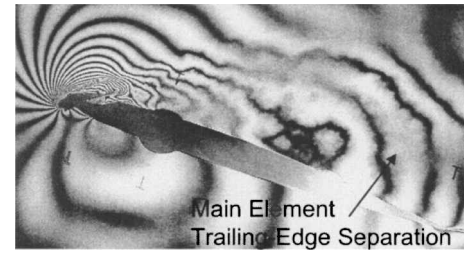

e) α = 19.5 deg

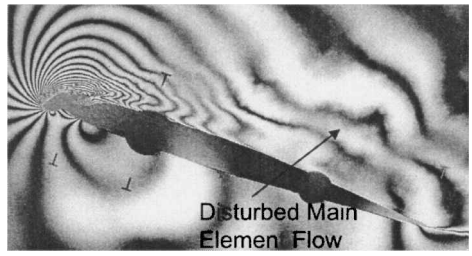

c) α = 19.0 deg

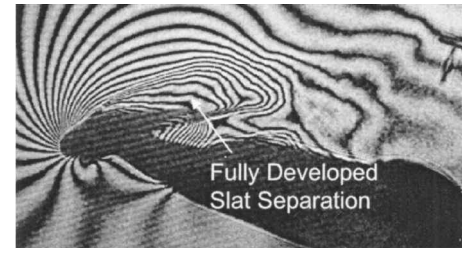

f) α = 19.5 deg, enlarged

Fig. 8 Interferograms showing instantaneous flow conditions during pitch oscillation of the slotted airfoil configuration RC(6)-08/210 at k = 0.05 and M = 0.30.

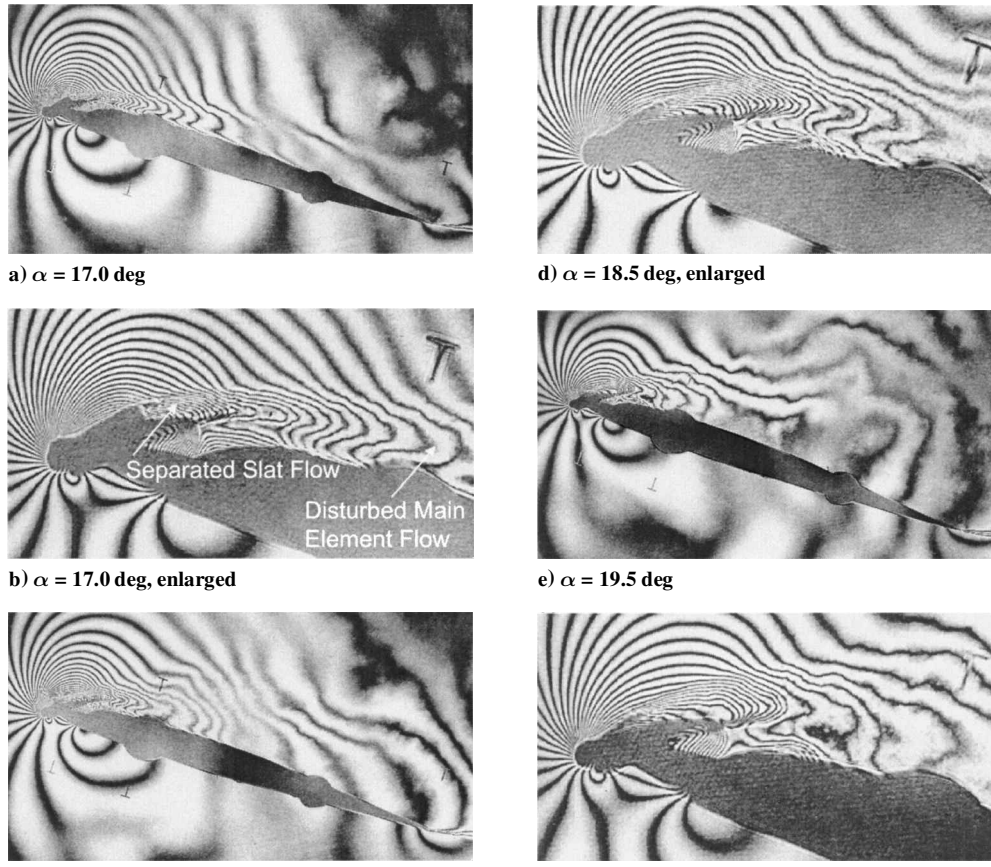

a) α = 17.0 deg

b) α = 17.0 deg, enlarged

c) α = 18.5 deg

d) α = 18.5 deg, enlarged

e) α = 19.5 deg

f) α = 19.5 deg, enlarged

Fig. 9 Interferograms showing instantaneous flow conditions during pitch oscillation of the slotted airfoil configuration RC(6)-08/210 at k = 0.05 and M = 0.35.

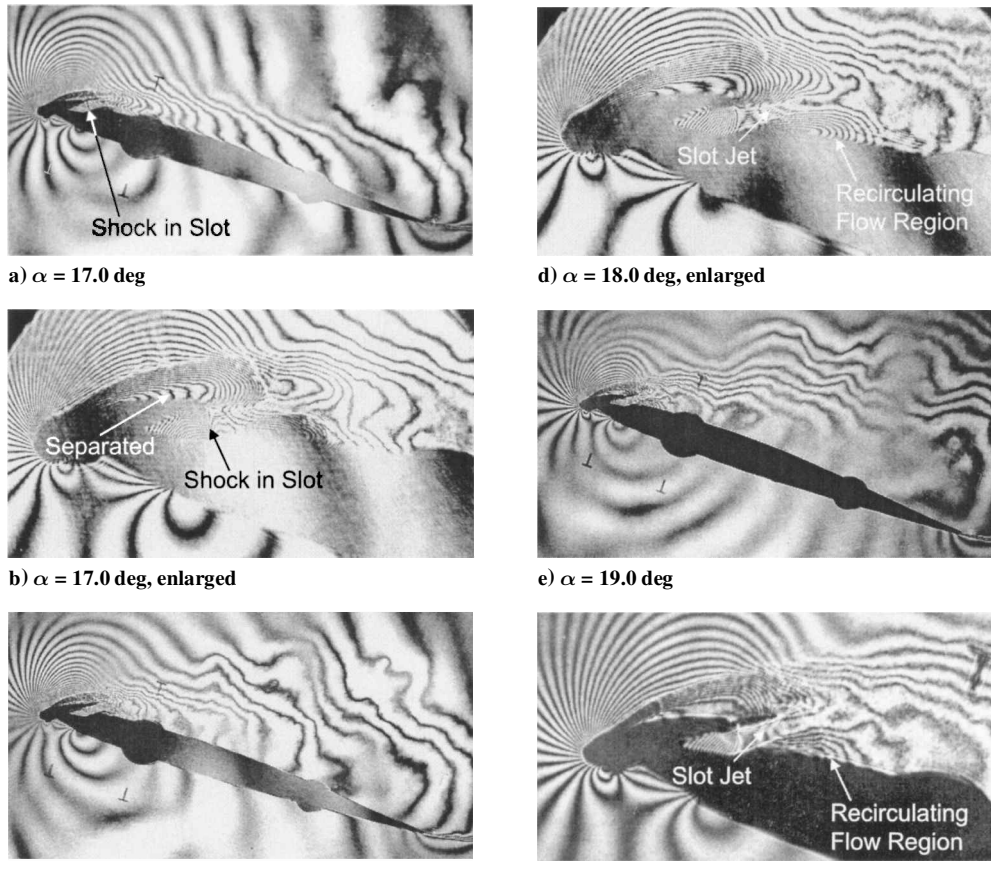

a) α = 17.0 deg

b) α = 17.0 deg, enlarged

c) α = 18.0 deg

d) α = 18.0 deg, enlarged

e) α = 19.0 deg

f) α = 19.0 deg, enlarged

Fig. 10 Interferograms showing instantaneous flow conditions during pitch oscillation of the slotted airfoil configuration RC(6)-08/210 at k = 0.05 and M = 0.40.

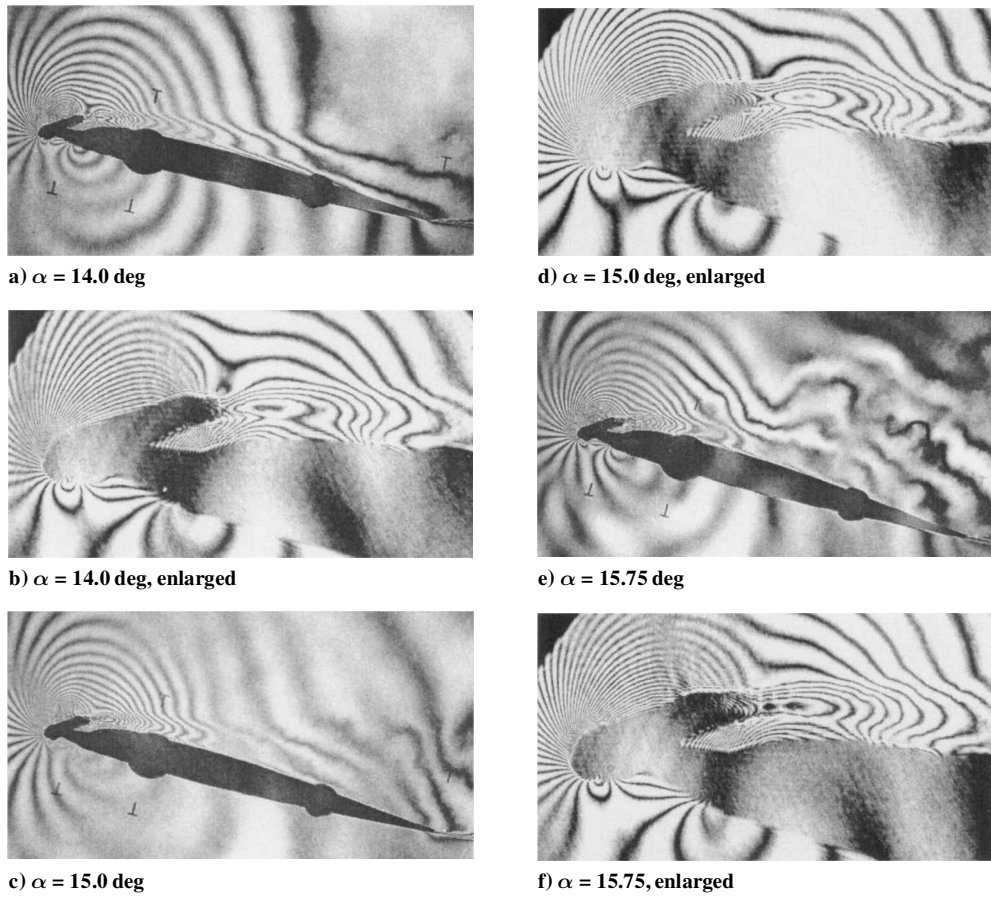

a) α = 14.0 deg

d) α = 15.0 deg, enlarged

b) α = 14.0 deg, enlarged

e) α = 15.75 deg

c) α = 15.0 deg

f) α = 15.75, enlarged

Fig. 11 Interferograms showing instantaneous flow conditions in steady flow over the slotted airfoil configuration RC(6)-08/210 at k = 0.0 and M = 0.40.

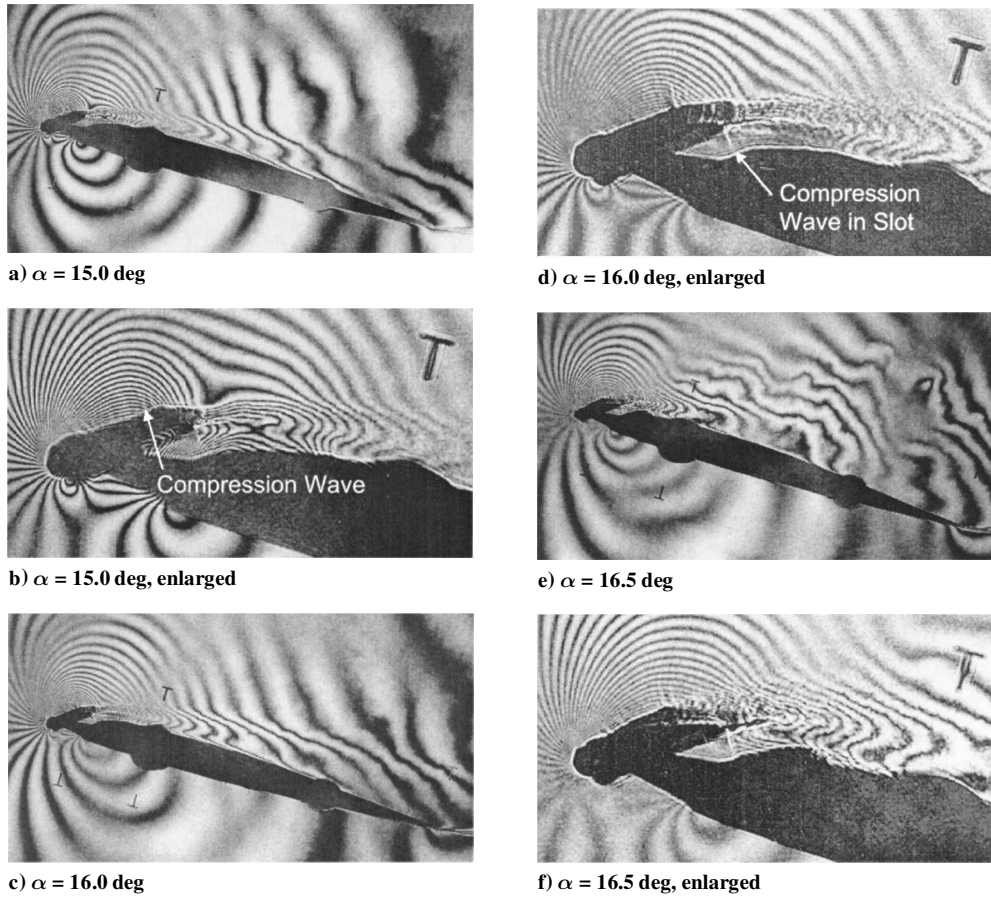

a) α = 15.0 deg

d) α = 16.0 deg, enlarged

b) α = 15.0 deg, enlarged

e) α = 16.5 deg

c) α = 16.0 deg

f) α = 16.5 deg, enlarged

Fig. 12 Interferograms showing instantaneous flow conditions during pitch oscillation of the slotted airfoil configuration RC(6)-08/210 at k = 0.025 and M = 0.40.

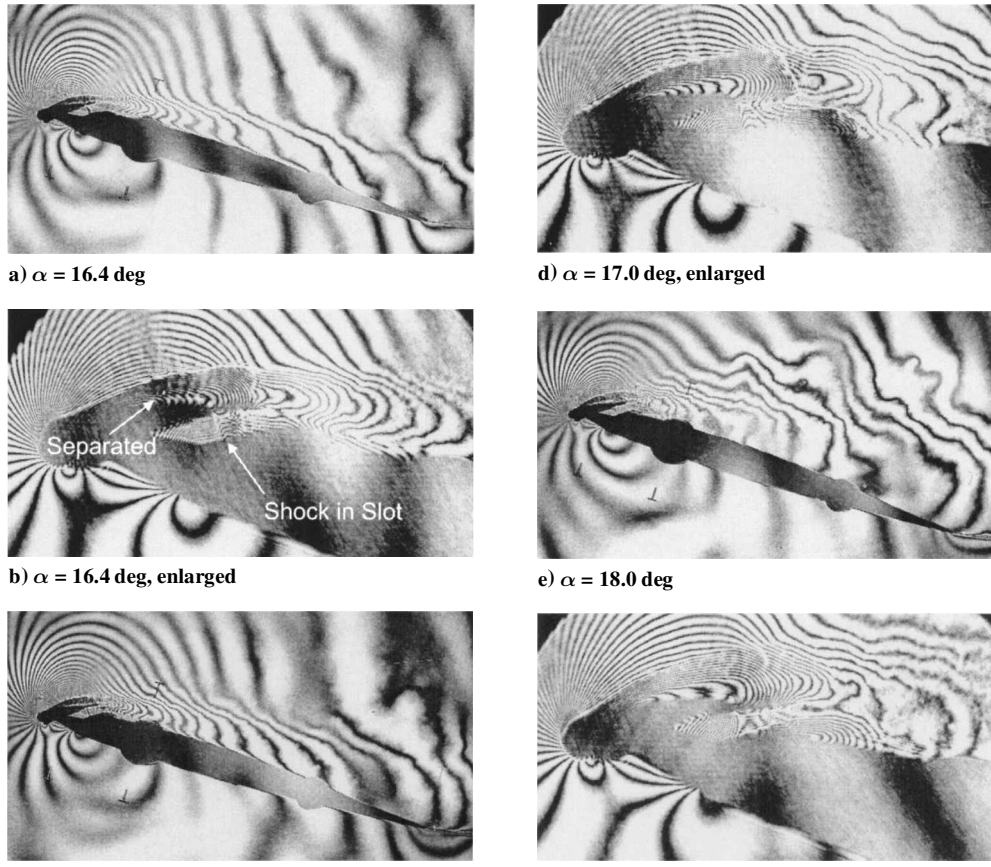

a) α = 16.4 deg

b) α = 16.4 deg, enlarged

c) α = 17.0 deg

d) α = 17.0 deg, enlarged

e) α = 18.0 deg

f) α = 18.0 deg, enlarged

Fig. 13 Interferograms showing instantaneous flow conditions during pitch oscillation of the slotted airfoil configuration RC(6)-08/210 at k = 0.05 and M = 0.40.

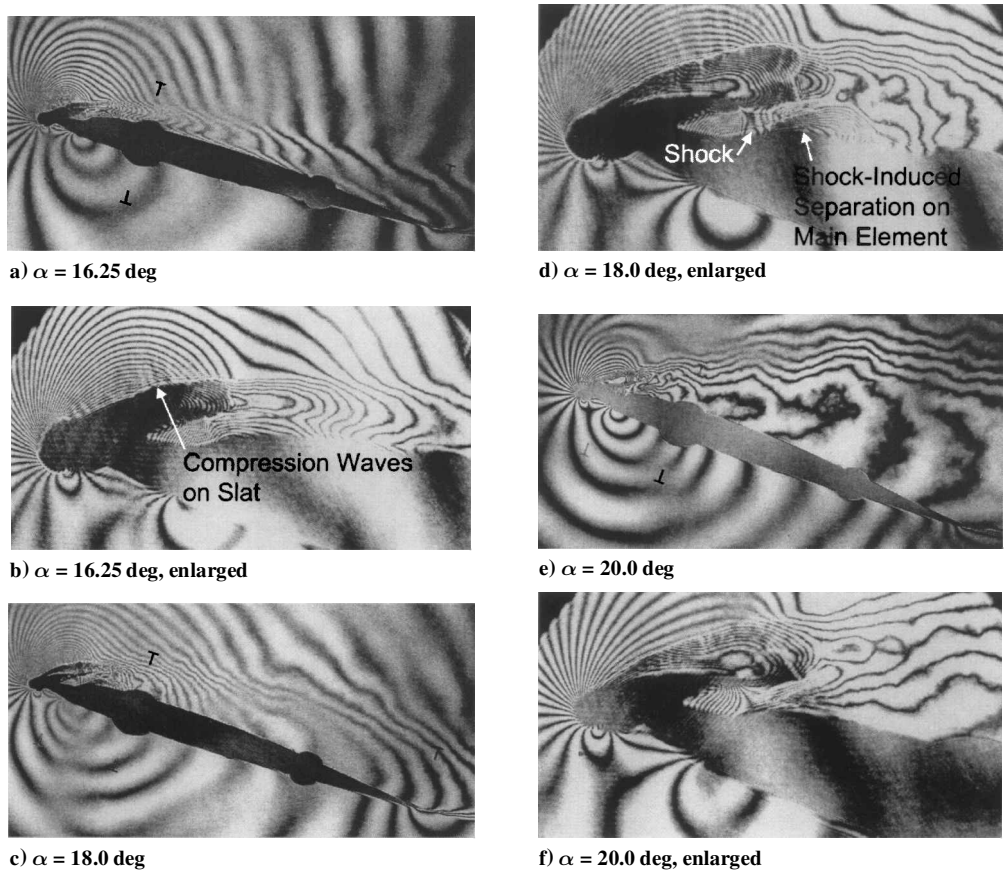

a) α = 16.25 deg

b) α = 16.25 deg, enlarged

c) α = 18.0 deg

d) α = 18.0 deg, enlarged

e) α = 20.0 deg

f) α = 20.0 deg, enlarged

Fig. 14 Interferograms showing instantaneous flow conditions during pitch oscillation of the slotted airfoil configuration RC(6)-08/210 at k = 0.075 and M = 0.40.

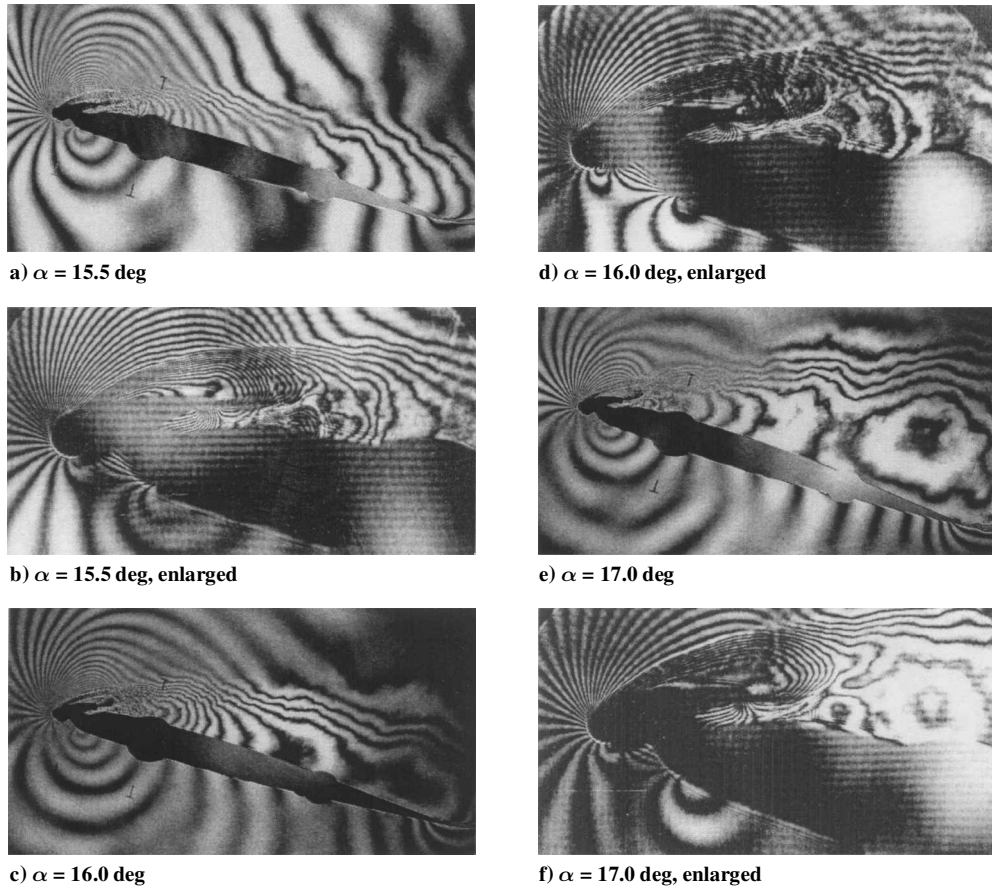

a) α = 15.5 deg

b) α = 15.5 deg, enlarged

c) α = 16.0 deg

d) α = 16.0 deg, enlarged

e) α = 17.0 deg

f) α = 17.0 deg, enlarged

Fig. 15 Interferograms showing instantaneous flow conditions during pitch oscillation of the slotted airfoil configuration RC(6)-08/106 at k = 0.05 and M = 0.40.

intersecting the surface in this area. (Because each fringe denotes a line of different constant density, it represents a different local Mach number.) The fringes downstream of the leading edge then turn back toward the surface of the airfoil, denoting the decrease in speed that occurs on the aft part of the airfoil. The presence of the boundary layer on the airfoil can be seen in the turning of these fringes parallel to the airfoil near the surface. By comparison, there is clear evidence of the presence of a dynamic stall vortex in Fig. 5c for $\alpha = 15.5$ deg (dynamic stall inception occurred at $\alpha = 14.0$ deg). In Fig. 5c, in contrast to Fig. 5a, the fringes now extend considerably into the outer flow before turning back toward the surface. Also, no boundary-layer fringes are seen in Fig. 5c. These fringes enclose a region of low pressure, a region that has been determined in earlier[9] studies to be in fact the dynamic stall vortex. As the angle of attack continues to increase, this dynamic stall vortex progressively grows and moves down the airfoil. Figure 5e shows this vortex near the trailing edge of the airfoil, at $\alpha = 16.25$ deg. Some of the fringe definition is lost when the vortex grows due to the mixing associated with the three-dimensional nature of the flow in the vortex.

This pattern occurs at progressively lower angle of attack as the freestream Mach number is increased. For example, at $M = 0.30$ and $k = 0.05$, dynamic stall inception is at $\alpha = 13.2$ deg; at $M = 0.35$ and $k = 0.05$, this occurs at $\alpha = 11.8$ deg; at $M = 0.40$ and $k = 0.05$, this occurs at $\alpha = 10.5$ deg. The results at $M = 0.40$ are presented in Figs. 6a–6f. Attached flow continues only up to $\alpha = 10.3$ deg at this Mach number (Fig. 6a). Note the increased number of fringes in Fig. 6 when compared to Fig. 5. Because there is a greater density range at this higher Mach number, the laser beam is phase shifted by a larger amount, and hence, there are more fringes appearing at this higher Mach number. There is a slight distortion seen in the enlarged images near the leading edge due to increased beam deflection arising from the larger density changes. However, the character of the flow at this high Mach number is quite similar to that seen at the lower Mach number: The increase in Mach number has caused dynamic stall onset at a much lower angle of attack ($\alpha = 10.5$ deg compared to $\alpha = 14.0$ deg). There is no strong visual evidence, such as a shock, of the increase in Mach number. At $\alpha = 11.5$ deg, the dynamic stall vortex has started moving down the airfoil, as can be seen in Fig. 6c. This dynamic stall vortex then continues to move down the airfoil and can be seen to be near the trailing edge in Fig. 6e, for $\alpha = 14.5$ deg. Thus, there is a clear influence of Mach number on dynamic stall onset for the basic RC(6)-08 airfoil, appearing as a decrease in the angle of attack at which dynamic stall occurs.

2. *Effect of Mach Number on RC(6)-08/210 Slotted Airfoil Performance*

Two slat/airfoil configurations were tested during the present study. Of the two, the RC(6)-08/210 demonstrated better performance during dynamic oscillation and will be analyzed first. Figure 7a presents an interferogram of the flow on the RC(6)-08/210 obtained at $M = 0.25$, $k = 0.05$, and $\alpha = 18.5$ deg, showing the flow on the slat and the main airfoil to be attached (the basic RC(6)-08 airfoil experienced dynamic stall at $\alpha = 14.0$ deg at these conditions). Note that the fringes on the slat in Fig. 7a are similar in nature to those observed near the leading edge of the basic RC(6)-08, with fringes normal to the surface near the leading edge of the slat and fringes curving back to the surface of the slat near the trailing edge. Note also that there are now two stagnation points visible in the interferogram, enclosed by the semicircular fringes seen on the lower surface in Fig. 7b. One is present on the slat, and an additional stagnation point is present on the main airfoil. Fringes are also apparent in the slot between the slat, the main airfoil, and in the slat wake, reflecting the large variation in velocity that is present in the flow through the slot.

The structure of the flow downstream of the trailing edge of the slat can be deduced from the fringe pattern in that region (Fig. 7b). Very close to the trailing edge of the slat, fringes intersecting the

upper surface of the slat turn downstream and extend in the downstream direction. These fringes then turn toward the airfoil and finally turn upstream, enclosing the region near the trailing edge of the slat, thus defining the wake of the slat. The influence of this wake on the density field above the main element can then be seen as a distortion of the fringe pattern over the rest of the main element of the airfoil (Fig. 7a). The fringes on the main airfoil near the trailing edge of the slat suggest an initial mild acceleration of the flow on the airfoil, followed by a mild deceleration downstream of the suction peak. Thus, most of the flow acceleration observed near the leading edge of the basic RC(6)-08 airfoil is now observed on the slat, with only secondary acceleration on the main airfoil.

This description is representative of the flow behavior over the multielement airfoil throughout most of the pitchup process from 0 to 20 deg during the $\alpha = 10 \text{ deg} + 10 \text{ deg} \sin \omega t$ oscillation cycle at $M = 0.25$. In fact, even at 20 deg (Fig. 7c), flow over the forward part of the main element remains fully attached; only the aft part of the airfoil shows any evidence of flow separation. This pattern of attached flow on the slat (Fig. 7d) remains during the downstroke, as can be seen in Figs. 7e and 7f, for $\alpha = 18.5$ deg. Thus, the flow over the slat has remained attached throughout the oscillation cycle, as has the flow over the forward portion of the main airfoil. In addition, there is no evidence of a dynamic stall vortex during any part of the cycle.

At $M = 0.30$, there is some change in the character of the flow at high angle during airfoil oscillation. At $\alpha = 18.0$ deg, although flow on the main airfoil is still fully attached in Fig. 8a, the first evidence of trailing-edge flow separation on the slat has appeared (Fig. 8b). This is seen as a jump in the fringes over the slat. By the time the airfoil has reached $\alpha = 19.0$ deg (Fig. 8c), separation on the slat is quite evident (Fig. 8d). The flow above the main airfoil is showing a strong disturbance in Fig. 8c; at $\alpha = 19.5$ deg (Figs. 8e and 8f), the slat separation is fully developed with the main element flow also nearly separated. Note also that this separated region on the slat is bounded by a series of fringes; this pattern will appear frequently and seems to be associated with the wake of the slat combining with the flow through the slot. Note that the flow on the main airfoil is separated over most of the airfoil, with an organized structure apparent in the separated region. This structure at first looked like a dynamic stall vortex. However, it became clear from study of the flow at this and higher angles that the structure is actually related to continuous shedding of vorticity from the leading edge (from where these fringes originate). For example, at $\alpha = 20$ deg, there was even more structure in the separated region about the airfoil (not shown), whereas a review of compressible dynamic stall on single element airfoils (see Ref. 9) shows no structure at all in the separated region in the deep dynamic stall state, that is, once the vortex has been shed. This supports the argument that the structure that is observed on the slotted airfoil at these high angles is not related to dynamic stall; instead, it is evidence of the continuing effect of the slat/slot flow control influence over the developing flow on the main airfoil.

At $M = 0.35$ and $k = 0.05$, the flow behavior has continued to change. At $\alpha = 17.0$ deg (Figs. 9a and 9b), the flow on the slat already is largely separated, and there is, also, distortion of the flow over the aft part of the main element. At $\alpha = 18.5$ deg (Figs. 9c and 9d), a flow disturbance is present over most of the main airfoil. Note that this flow disturbance is highly time dependent, but is not a dynamic stall vortex. Indeed, this structured flow remains on the airfoil at high angles of attack during the oscillation cycle and was seen in all of the interferograms recorded for this condition. For example, at $\alpha = 19.5$ deg (Figs. 9e and 9f) this structure continues to be seen. Note also that the closed region above the slat remains bounded by several fringes. The flow over the slat continues to maintain low pressure even though the flow over the main airfoil is highly disturbed. This continuation of low pressure on the slat even when the flow has separated in this unsteady condition is reminiscent of the attached flow that was observed on the nose of a deformable airfoil[11] during dynamic motion. In that case as well, the flow near the nose of the airfoil remained attached even at the highest angle of attack tested, and no dynamic stall vortex was observed at any time in the oscillation cycle. No dynamic stall vortex has been observed at any angle of attack in the present case as well.

At $M = 0.40$ and $k = 0.05$, major changes in the flow behavior are apparent. At $\alpha = 17.0$ deg (Fig. 10a), the flow on the main airfoil becomes disturbed. Further, not only has the flow on the slat separated, but, also, a normal shock has developed in the exit region of the slot between the slat and the main airfoil. The dramatically different fringe pattern and the sharp discontinuity in the fringes observed in Fig. 10b confirm the presence of a shock. Signs of separation are also evident at the foot of the shock. The presence of the shock in the slot of a slotted RC(6)-08/210 airfoil clearly demonstrates the type of change that occurs due to even modest freestream Mach number change. At $\alpha = 18.0$ deg (Fig. 10c), the flow on the slat shows increasing separation; the flow on the main airfoil has become highly disturbed. Note that the shock has weakened in the slot as flow separation relieves the flow acceleration (Fig. 10d). A recirculation region has developed at the foot of the shock near the slot exit, which can be seen more clearly at $\alpha = 19.0$ deg (Figs. 10e and 10f). The flow on the slat shows full separation in Fig. 10f. Also, a jet of air appears in the slot, proceeding immediately away from the surface of the airfoil, and the disturbed flow over the main element has dramatically thickened. However, note the continuing presence of structure in the flow over the main airfoil. This indicates that even under these severe conditions, the slat/slot combination is continuing to energize the flow on the main airfoil through the slot jet. Also, note that no dynamic stall vortex has appeared, even for this strongly compressible flow condition. The presence of the shock in the slot does not seem to affect the performance of the slat.

These flow features lead to the questions whether the slat could be designed to operate choked under the worst flow condition and whether the jet can be directed as a wall jet to control the main element boundary layer. The answers to these questions are still elusive because the slat surface boundary layer changes and develop under vastly different flow conditions due to the range of Mach numbers and angles of attack a rotor is subjected to. Furthermore, the slat flow can separate at lower Mach numbers and angles of attack if it is optimized for the higher Mach number conditions. There is also very little choice on the slot geometry design because the slot lower surface and the main airfoil have to be matched and are not designed for dynamic stall and its control. Hence, there is at best a very limited range of conditions where the slot can be profiled for the best performance.

In summary, there are noteworthy changes in the physics of the unsteady stall process on the RC(6)-08/210 airfoil as Mach number increases. For an example of the effect of this change in physics at a specific angle of attack, compare Figs. 8a, 9c, and 10c. At $k = 0.05$, $M = 0.30$, and $\alpha = 18$ deg (Fig. 8a), the flow on the main element is clearly attached, and only slight separation is present on the slat. At $M = 0.35$ and $\alpha = 18$ deg (Fig. 9c), the flow on the slat shows separation, and the flow on the main element is disturbed. At $M = 0.40$ and $\alpha = 18$ deg (Fig. 10c), the slat flow is fully separated, and there is large-scale separation on the main element. Even for strongly compressible conditions, the absence of a dynamic stall vortex in the interferometric images of the flow demonstrates that the proper use of a slat can eliminate the dynamic stall vortex, a major goal of dynamic stall flow control.

3. *Effect of Frequency on Dynamic Stall of the RC(6)-08/210 Airfoil*

There is an equally large effect of change in oscillation frequency, which can be seen at $M = 0.40$. In steady flow ($k = 0.0$), the flow over the RC(6)-08/210 is attached everywhere on the slat and the main airfoil at $\alpha = 14.0$ deg (Figs. 11a and 11b). At $\alpha = 15.0$ deg (Figs. 11c and 11d), some disturbance is observed near the trailing edge of the main airfoil. At $\alpha = 15.75$ deg (Figs. 11e and 11f), the flow on the slat starts to separate, and the flow near the rear of the main airfoil also experiences separation, even as compression waves appear above the slat.

At $k = 0.025$, the flow is attached on both the airfoil and the slat up to $\alpha = 15.0$ deg (Figs. 12a and 12b), with compression waves visible on the slat. At $\alpha = 16.0$ deg (Figs. 12c and 12d), the compression waves above the slat are stronger, and separation of the flow on the

slat has begun, although there is no separation on the main airfoil. A compression wave appears on the lower surface of the slat, and flow on the main element remains attached. At $\alpha = 16.5$ deg (Figs. 12e and 12f), the flow on the main element of the airfoil shows significant disturbance. There is some delay in the development of the flow when compared to $k = 0.0$; no dynamic stall vortex is observed.

At $k = 0.05$, the flow is fully attached at $\alpha = 15.0$ deg (not shown), with only minor visible evidence of compressibility seen. At $\alpha = 16.0$ deg (not shown), a compression wave develops on the upper surface of the slat, and the slat flow starts to separate. At $\alpha = 16.4$ deg (Figs. 13a and 13b), this compression wave can been seen on the rear upper surface of the slat, and the presence of a shock in the slot near the end of the slat has become quite apparent. This persists through $\alpha = 17.0$ deg (Figs. 13c and 13d), while flow over the main airfoil shows some disturbances, but only a mild separation. However, at $\alpha = 17.2$ deg (not shown), there is a large disturbance over the aft portion of the main airfoil, as well as at the exit of the slot. At $\alpha = 17.8$ deg (not shown), much of the main airfoil shows a strong disturbance; however, the shock in the slot weakens. By $\alpha = 18.0$ deg (Figs. 13e and 13f), the shock has disappeared, and flow on the main airfoil is highly disturbed. Note that no dynamic stall vortex was observed at any angle at this test condition.

At $k = 0.075$ and $\alpha = 15.0$ deg (not shown), the flow remains fully attached to both the slat and the main airfoil, with little evidence of compressibility. At $\alpha = 16.0$ deg (not shown), compression waves form above and below the slat, although the flow on the main airfoil is undisturbed. At $\alpha = 16.25$ deg (Figs. 14a and 14b), these compression waves become more pronounced both above and below the slat, and the flow over the slat starts to separate. At $\alpha = 16.5$ deg (not shown), the flow on the slat separates, and a shock appears in the slot, but no separation is apparent on the main airfoil. At $\alpha = 18.0$ deg (Figs. 14c and 14d), the shock in the slot is quite evident, some separation downstream of the shock is present on the main airfoil, and some disturbance appears in the flow over it. At $\alpha = 20$ deg, the highest α tested (Figs. 14e and 14f), the shock has disappeared, the flow on the slat is fully separated, and the flow on the main airfoil is mostly separated. The separated flow on the slat is still bounded by several fringes, and the structure in the separated region on the main airfoil is clear from the fringe pattern appearing there. Thus, the flow over the main airfoil continues to remain energized, even at 20-deg angle of attack, showing that the slat is still imposing control over this flow even at this very high angle of attack.

Thus, compressibility effects on the slotted airfoil are strongly dependent on the rate of airfoil oscillation. Even at $M = 0.40$, there is little visible evidence of compressibility (shocks, compression waves, etc.) during angle-of-attack change in steady flow. This contrasts sharply with the character of the flow as the oscillation rate is increased. In particular, a shock develops in the slot of the multielement airfoil at $k = 0.05$ and $k = 0.075$, and this shock plays an important role in the development of the flow at high angle of attack. This type of behavior cannot be extrapolated from steady flow results. It is very important to note that no dynamic stall vortex was observed on the RC(6)-08/210 airfoil at any Mach number or reduced frequency tested in this study.

B. Effect of Change in Slat Configuration

A second leading-edge slat configuration was evaluated as part of the present research program. The RC(6)-08/106 configuration has the same profile for the slat and the main airfoil as RC(6)-08/210, but the RC(6)-08/106 configuration has a different reference position and angle for the leading-edge slat (see Ref. 5 for details of the slat design). The RC(6)-08/106 configuration experienced a somewhat lower $C_{l_{\max}}$ in steady flow tests (see Fig. 2); more important, as will be seen, the dynamic stall related performance at high Mach number is much different from the RC(6)-08/210.

Consider the effect of Mach number for this new slat configuration. These effects will be compared to the RC(6)-08/210 results already discussed. Figures 15 show images at $M = 0.40$ for visual comparison. At $M = 0.25$ and $k = 0.05$, the RC(6)-08/210 showed fully attached flow at $\alpha = 18.5$ deg. By comparison, the slat on RC(6)-08/106 had already separated at $\alpha = 17.5$ deg. In fact, although the RC(6)-08/210 flow stayed attached at all angles up to $\alpha = 20$ deg, both the slat and the main RC(6)-08/106 airfoil show flow separation at $\alpha = 19.0$ deg. For $M = 0.30$ and $k = 0.05$, at $\alpha = 17.0$ deg, the RC(6)-08/210 flow was fully attached; however, the RC(6)-08/106 slat has already separated at this angle, and a strong disturbance is seen in the main airfoil flow. At $\alpha = 18.0$ deg, the slat and the main airfoil of the RC(6)-08/106 have separated, whereas the flow over the RC(6)-08/210 experienced only moderate separation on the slat and no separation on the main airfoil. At $M = 0.35$ and $k = 0.05$, separation has already begun on the slat of the RC(6)-08/106 by $\alpha = 14.5$ deg, although the main airfoil flow is still attached. At $\alpha = 16.5$ deg, the flow on the slat and the main airfoil show full separation. By comparison, the flow on the RC(6)-08/210 at $\alpha = 17.0$ deg has only a small region of separating flow on the slat, with flow attached to the main airfoil over most of its length.

The interferograms obtained for the RC(6)-08/106 at $M = 0.40$ and $k = 0.05$ show an interesting development in the flow on this airfoil. Flow on the slat starts to separate at $\alpha = 13.5$ deg (not shown); however, the flow on the main airfoil remains attached up to $\alpha = 14.5$ deg (not shown). At $\alpha = 15.5$ deg (Figs. 15a and 15b), all of the fringes near the main airfoil surface over the full length of the airfoil have turned normal to the surface, a pattern often seen near the leading edge of single-element airfoils before initiation of a dynamic stall vortex. However, during dynamic stall vortex formation on a single-element airfoil, this pattern only appears near the leading edge of the airfoil and then progresses toward the trailing edge. In the present case, the turning of the fringes has appeared in all of the fringes on the main airfoil virtually simultaneously. This is followed by a progressive decrease in the number of fringes on the upper surface (see Figs. 15c and 15d, $\alpha = 16.0$ deg, and Figs. 15e and 15f, $\alpha = 17.0$ deg), suggesting a progressive loss of suction and, hence, lift as the angle of attack increases. This suggests that rather than a conventional dynamic stall vortex, the RC(6)-08/106 experiences a progressive loss of lift, with a slow movement of the center of pressure, thus making the slotted airfoil dynamic separation a mild event compared to that observed on single-element airfoils. Note that no shock has formed on either the slat, the main airfoil, or in the slot at this condition. In strong contrast to the flow on the RC(6)-08/210, note also that at $\alpha = 17.0$ deg the RC(6)-08/210 airfoil is still operating with attached flow on the main airfoil, as can be seen in Fig. 10a.

Thus, although the RC(6)-08/106 airfoil does not perform as effectively as the RC(6)-08/210 does in controlling dynamic stall, the results presented show that when the slotted airfoil configuration does stall dynamically, the stall process is less severe than that seen on a single-element airfoil at the same conditions.

C. Pressure Distributions

As discussed in Ref. 10, interferograms are maps of the instantaneous density field on and above the airfoil; each fringe is a line of constant density and, therefore, in the inviscid flowfield, a line of constant pressure. Therefore, to the accuracy of the boundary-layer assumption that pressure does not change across the boundary layer, instantaneous pressure distributions on the airfoil surface can be obtained by extrapolation of the fringe contours to the surface. An example of such a plot can be seen in Fig. 16, which presents the pressure distributions on the RC(6)-08 airfoil at various angles of attack during oscillation at $M = 0.30$, $k = 0.05$, and $\alpha = 10 \text{ deg} + 10 \text{ deg} \sin \omega t$. Note that dynamic stall occurs at $\alpha = 12.75$ deg for these conditions; the pressure distribution at $\alpha = 14.0$ deg shows the character of the flow at an angle above the dynamic stall angle during the period when the dynamic stall vortex still remains on the airfoil.

Compare these results to the pressure distributions for the RC(6)-08/210 airfoil, as shown in Fig. 17 for $M = 0.30$. At $\alpha = 16.0$ deg, the flow is fully attached (Fig. 17a); indeed, at $\alpha = 19.0$ deg, the flow is still mostly attached (Fig. 17b). The effect of Mach number change can be seen in Fig. 18. A representative pressure distribution for this airfoil at $M = 0.30$ can be seen in Fig. 18a, for $k = 0.05$

and $\alpha = 16$ deg. The corresponding pressure distribution for this airfoil at $M = 0.35$, $k = 0.05$, and $\alpha = 16$ deg is shown in Fig. 18b and at $M = 0.40$ in Fig. 18c, thus demonstrating the effect of Mach number on the instantaneous pressure distribution on this airfoil. The RC(6)-08/106 airfoil did not perform as effectively in dynamic stall, as discussed earlier. This is reflected in the pressure distributions shown in Fig. 19, for $M = 0.30$, $k = 0.05$, and various angles of attack. Note the drop in peak suction as the angle of attack increases from $\alpha = 16$ to $\alpha = 17$ deg (Figs. 19a and 19b). Also note that there is no evidence of a dynamic stall vortex in the pressure distribution at $\alpha = 17$ deg, even though there is a loss in suction at the leading edge. In fact, although the pressure distribution at $\alpha = 20$ deg (Fig. 19c) shows stalled flow on both the slat and the main airfoil, there is no evidence of dynamic stall at any time in the oscillation cycle at these conditions, based on the interferogram images obtained for this condition.

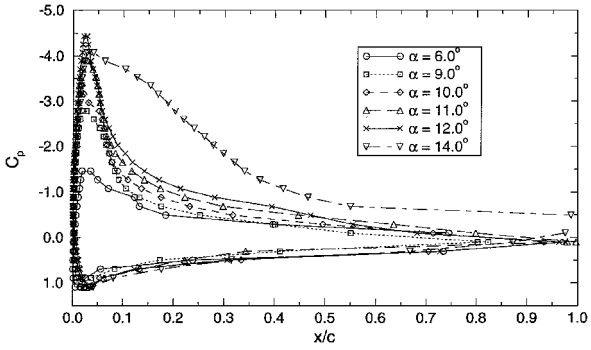

Fig. 16 Instantaneous pressure distributions on RC(6)-08 airfoil during dynamic motion as obtained from interferograms, $M = 0.3$, $k = 0.05$, and $\alpha = 10$ deg + 10 deg sin ωt.

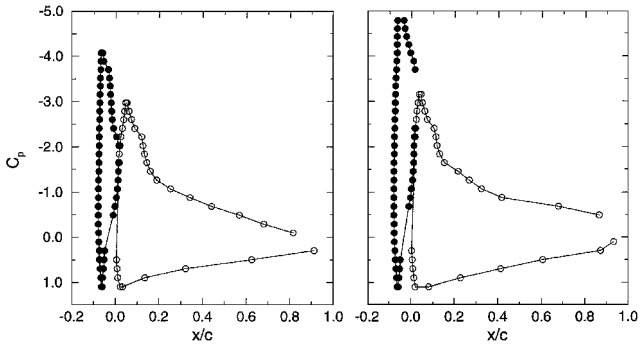

a) $\alpha = 16.0$ deg **b) $\alpha = 20.0$ deg**

Fig. 17 Instantaneous pressure distributions on the RC(6)-08/210 airfoil during dynamic motion at $M = 0.35$, $k = 0.05$, $\alpha = 10$ deg + 10 deg sin ωt.

Variation of the minimum C_p in the instantaneous pressure distributions as α is increased has been a good indicator of the status of the dynamic flow on oscillating single-element airfoils.[11] In the present case, this development is presented in Fig. 20. Here, the $C_{p_{\min}}$ for the NACA0012 and the RC(6)-08 are compared to the $C_{p_{\min}}$ on the slat for the two slat configurations for $M = 0.30$, 0.35, and 0.40. Note that the $C_{p_{\min}}$ for the RC(6)-08 airfoil is clearly less than that for the NACA 0012, no doubt reflecting the improved high Mach number performance of the RC(6)-08. However, note also that at $M = 0.40$, the drop in $C_{p_{\min}}$ associated with dynamic stall occurs earlier for the RC(6)-08 than for the NACA0012 for these conditions. The delay in dynamic stall that occurs for the RC(6)-08/106 can also be seen in Fig. 20 for $M = 0.30$. Note that for the RC(6)-08/106, at all of the angles of attack tested, there is a reduction in $C_{p_{\min}}$ compared to the basic RC(6)-08; this reduction in $C_{p_{\min}}$ is even more pronounced for the RC(6)-08/210. As shown in Fig. 20, $C_{p_{\min}}$ on the RC(6)-08/210 continues to increase as the angle of attack increases almost all of the way up to $\alpha = 20$ deg, and only then does the $C_{p_{\min}}$ show a decrease. The absence of a dynamic stall vortex in this case has been demonstrated by the interferograms discussed earlier in this paper. The corresponding development of $C_{p_{\min}}$ at $M = 0.40$ is also shown in Fig. 20; the basic RC(6)-08 continues to show a lower $C_{p_{\min}}$ than the NACA0012, but also shows a lower angle of dynamic stall inception. The RC(6)-08/210 again shows a delay in reaching maximum $C_{p_{\min}}$, with a gradual decrease at high angle of attack. Again, interferograms for these conditions show this dropoff in $C_{p_{\min}}$ is not associated with a dynamic stall vortex, suggesting that drop in $C_{p_{\min}}$ is an indicator of dynamic stall onset only for single-element airfoils.

D. Effect of Reynolds Number

The present test was performed at $Re = 0.4 \times 10^6$–0.72×10^6. In Fig. 21, the $C_p(x)$ distribution for the RC(6)-08/210 obtained from an interferogram created in the present test is shown for $Re = 0.7 \times 10^6$ and $k = 0.0$ and is compared to data obtained using pressure taps at 5.0×10^6 (Ref. 5). There is a clear difference between these results. Part of the difference can be attributed to the difference in Reynolds number; however, not all of the difference may be due to the change in viscous–inviscid interaction associated

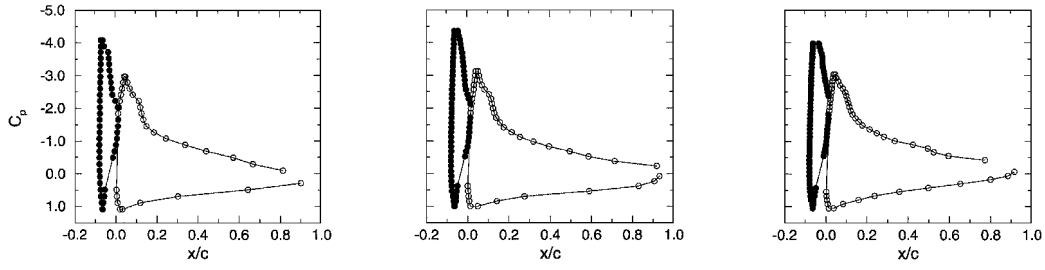

a) $M = 0.30$ **b) $M = 0.35$** **c) $M = 0.40$**

Fig. 18 Instantaneous pressure distributions on the RC(6)-08/210 airfoil during dynamic motion at $k = 0.05$, $\alpha = 10$ deg + 10 deg sin ωt, $\alpha = 16.0$ deg.

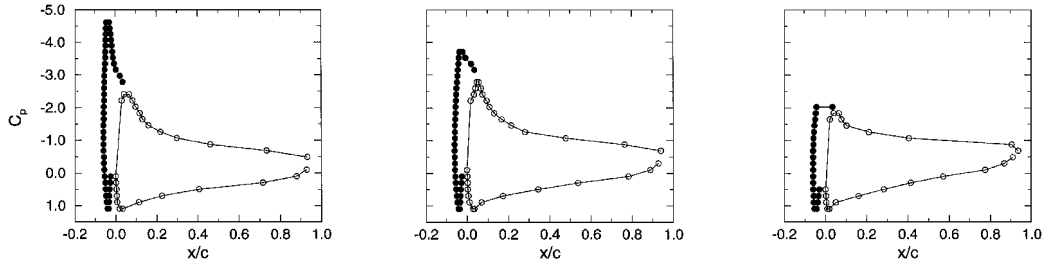

a) $\alpha = 16.0$ deg **b) $\alpha = 17.0$ deg** **c) $\alpha = 20$ deg**

Fig. 19 Instantaneous pressure distributions on the RC(6)-08/106 airfoil during dynamic motion at $M = 0.30$, $k = 0.05$, $\alpha = 10$ deg + 10 deg sin ωt.

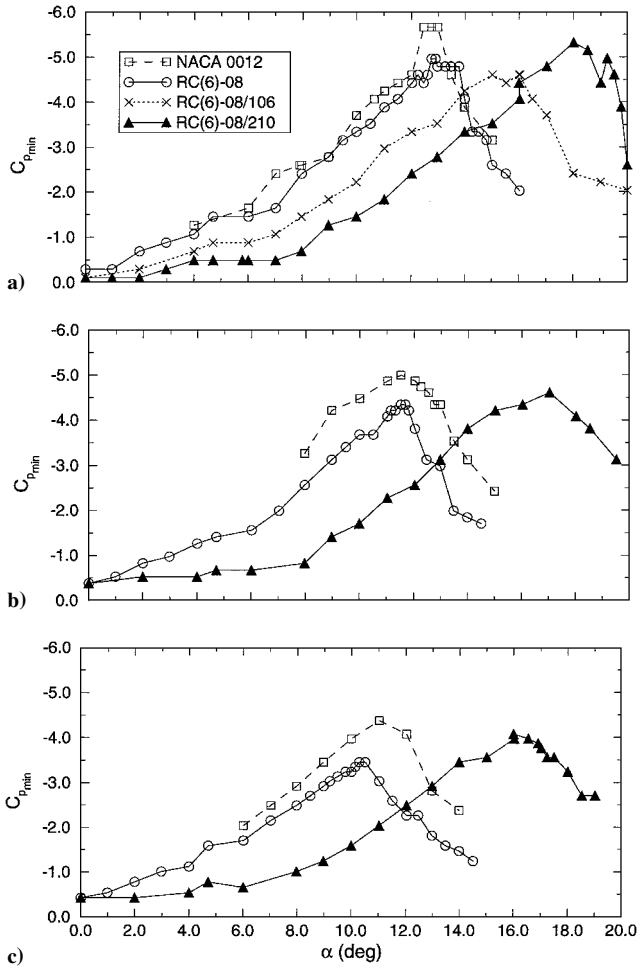

Fig. 20 Development of $C_{p_{min}}$ on basic and slatted airfoils as function of angle of attack for various Mach numbers.

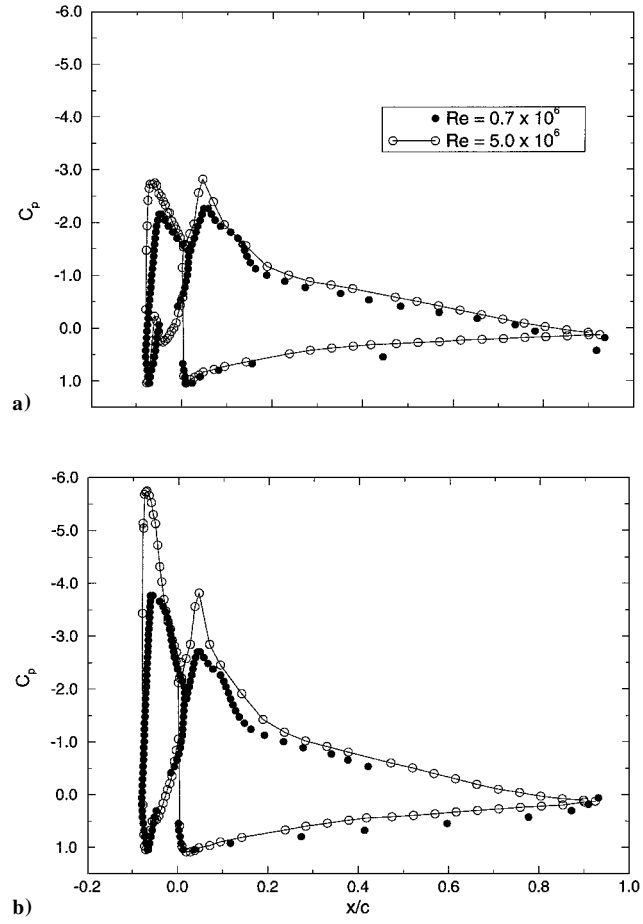

Fig. 21 Comparison of pressure distributions obtained from interferograms at $Re = 0.7 \times 10^6$ to pressure distributions obtained from pressure taps (Ref. 5) at $Re = 5.0 \times 10^6$ at $M = 0.4$, and $k = 0$: a) $\alpha = 10.0$ deg and b) $\alpha = 15.5$ deg.

with Reynolds number change. For example, at a chord Reynolds number of 0.5×10^6, the slat is operating at a Reynolds number of 0.05×10^6, a Reynolds number low enough that laminar flow separation may be dominating the development of flow over the slat. Thus, quantitative comparison between 0.7×10^6 and 5.0×10^6 results may not be possible for steady flow.

By comparison, suppression of the dynamic stall vortex seems to be less sensitive to Reynolds number effects. Certainly, this has been demonstrated in the case of slotted airfoils during dynamic stall tests: Slotted airfoils have now been tested at $M = 0.185$ and $Re = 2.5 \times 10^6$ (Ref. 4) as well as $M \cong 0$ and $Re = 0.2 \times 10^6$ (Ref. 11), with singular success at suppression of dynamic stall. As shown in the present test, the slotted airfoil concept has now been demonstrated to work for Mach numbers as high as $M = 0.40$, the first dynamic stall suppression technique to have worked at such a high Mach number.

E. Effect of Reynolds Number on Vorticity Dynamics

A dominant factor in dynamic stall development is vorticity dynamics, as discussed in detail in Ref. 12. In the present case, the pressure distribution on the slat is much stronger than that on the main airfoil, resulting in most of the vorticity being produced on the slat. As has been seen in the various interferograms presented earlier in this paper, the slat flow shows separation, but this separated region is bounded throughout the oscillation cycle, thus maintaining attached flow at the nose of the airfoil throughout the oscillation cycle. At the same time, vorticity is being shed into the wake from the slat. This shedding of vorticity into the wake of the slat seems to reenergize the flow on the main airfoil; at the same time, sufficient vorticity is shed into the wake to permit the slotted airfoil to pass through the oscillation cycle without producing a dynamic stall vortex. This characteristic of the slat seems to be independent of Reynolds number, as well as compressibility effects, thus making the slotted airfoil concept a robust dynamic stall control technique.

IV. Concluding Remarks

1) Two slotted airfoils designed for high lift in steady flow at conditions appropriate for helicopter applications have been tested for dynamic stall behavior at compressible flow conditions and compared to corresponding results for the basic single-element airfoil used as a basis for the slotted airfoil designs.

2) One of these slotted airfoils, RC(6)-08/210, operated throughout the range of Mach numbers representative of helicopter flight without experiencing a dynamic stall vortex at any condition tested, thus demonstrating the value of such a configuration for application to future helicopters.

3) A detailed discussion of the flow on the optimum slot design showed that the design was effective in suppressing the dynamic stall vortex, even at the high Mach numbers that have negated the effectiveness of many flow control concepts.

4) Significant compressibility effects were observed, including a strong shock appearing in the slot for certain dynamic conditions. This shock played an important role in the development of the flow at high angle of attack and shows the type of flow condition that only occurs during dynamic motion at compressible flow conditions.

5) Flow separation on the slat and main airfoil element progressively increased as the Mach number increased, but no dynamic stall vortex was observed at any of the conditions tested.

6) A comparison with the basic single-element airfoil, as well as a second slat design, showed the improvements that can be attained through effective slat design.

7) The slot-jet continued to energize the main element boundary layer even after the slat stalled. This suggests the possibility that there may be some special slot geometries that are most efficient for this task. However, the many conflicting requirements of the main element leading-edge geometry for the wide ranging conditions of the rotor need to be considered carefully if this effort is to succeed.

8) Instantaneous pressure distributions were presented showing the influence of slat design on the suction peak that occurs in the pressure distribution.

9) A discussion of Reynolds number effects was presented that indicated that the dynamic stall suppression resulting from use of the slat concept also seems to be insensitive to changes in Reynolds number.

References

[1]Carr, L. W., "Progress in Analysis and Prediction of Dynamic Stall," *Journal of Aircraft*, Vol. 25, No. 1, 1988, pp. 6–17.

[2]Carr, L. W., and McCroskey, W. J., "A Review of Recent Advances in Computational and Experimental Analysis of Dynamic Stall," Proceedings of the International Union of Theoretical and Applied Mechanics, Symposium on Fluid Dynamics of High Angle of Attack, Springer-Verlag, Berlin, Sept. 1992, pp. 1–33.

[3]Carr, L. W., and Chandrasekhara, M. S., "Compressibility Effects on Dynamic Stall," *Progress in Aerospace Sciences*, Vol. 32, No. 6, 1996, pp. 523–573.

[4]Carr, L. W., and McAlister, K. W., "The Effect of a Leading-Edge Slat on the Dynamic Stall of an Oscillating Airfoil," AIAA Paper 83-2533, Oct. 1983.

[5]Noonan, K. W., Allison, D. O., and Stanaway, S., "Investigation of a Slotted Rotorcraft Airfoil at Mach Numbers from 0.20 to 0.88 at Full-Scale Reynolds Numbers," American Helicopter Society Aeromechanics Specialists Conf. Jan. 1994, Paper 4, 5.

[6]Noonan, K. W., "Aerodynamic Characteristics of a Rotorcraft Airfoil Designed for the Tip Region of a Main Rotor Blade," NASA TM 4264, 1991.

[7]Carr, L. W., and Chandrasekhara, M. S., "Design and Development of a Compressible Dynamic Stall Facility," *Journal of Aircraft*, Vol. 29, No. 3, 1992, pp. 314–318.

[8]Brock, N. J., Chandrasekhara, M. S., and Carr, L. W., "A Real Time Interferometry System for Unsteady Flow Measurements," *ICIASF '91 Record*, IEEE Publ. 91CH3028-8, 1991, Inst. of Electrical and Electronics Engineers, New York, pp. 423–430.

[9]Carr, L. W., Chandrasekhara, M. S., and Brock, N. J., "Quantitative Study of Unsteady Compressible Flow on an Oscillating Airfoil," *Journal of Aircraft*, Vol. 31, No. 4, 1994, pp. 892–898.

[10]Chandrasekhara, M. S., Wilder, M. C., and Carr, L. W., "Unsteady Stall Control Using Dynamically Deforming Airfoils," AIAA Paper 97-2236, June 1997.

[11]DeHughes, P. P., McAlister, K. W., and Tung, C., "Effect of an Extendable Slat on the Stall Behavior of a VR-12 Airfoil," NASA TP-3407, 1993.

[12]Reynolds, W. C., and Carr, L. W., "Review of Unsteady, Driven, Separated Flows," AIAA Paper 85-0527, March 1985.